

Eastward expansion of the Tibetan Plateau by crustal flow and strain partitioning across faults

Qi Yuan Liu¹, Robert D van der Hilst², Yu Li¹, Hua Jian Yao³, Jiu Hui Chen¹,
Biao Guo¹, Shao Hua Qi¹, Jun Wang¹, Hui Huang², Shun Cheng Li¹

- 1) State Key Laboratory of Earthquake Dynamics, Institute of Geology, CEA, China
- 2) Department of Earth, Atmospheric and Planetary Sciences, MIT, USA
- 3) Laboratory of Seismology and Physics of Earth's Interior, USTC, China

Supporting Online Material

1. Method and numerical tests: Teleseismic receiver function (RF) inversion, which is now routinely used to constrain crustal structures, is subject to substantial non-uniqueness¹ because RFs are sensitive only to wavespeed contrasts and determination of their depth relies on a priori information about propagation speed.

The problem of non-uniqueness can be mitigated through joint inversion of RF and surface waves dispersion data²⁻⁵, with the latter constraining crustal wavespeed variations. Surface wave dispersion can be extracted from earthquake recordings and also from ambient seismic noise cross-correlation functions⁶⁻¹⁰, thus motivating joint inversion of RF and ambient noise data. Liu et al.¹¹ proposed a Bayesian method to invert RF and Rayleigh-wave phase-velocity dispersion estimated for ambient noise tomography (ANT)¹²⁻¹³. In concept, RFs are then considered as a priori information for ANT, and vice versa. An important advantage of joint RF-ANT inversion is that short-period phase velocity dispersion (< 20 s), which constrains the shallow structures beneath receivers, is obtained easily from ambient noise cross-correlation.

The joint RF-ANT inversion method¹¹ is performed in the complex spectral domain. The objective function is constructed as

$$S(\mathbf{m}) = \frac{1}{2} \left\{ [\mathbf{g}_{RF}(\mathbf{m}) - \mathbf{d}_{RF}]^* \mathbf{C}_{RF}^{-1} [\mathbf{g}_{RF}(\mathbf{m}) - \mathbf{d}_{RF}] + [\mathbf{g}_{SF}(\mathbf{m}) - \mathbf{d}_{SF}]^* \mathbf{C}_{SF}^{-1} [\mathbf{g}_{SF}(\mathbf{m}) - \mathbf{d}_{SF}] + (\mathbf{m} - \mathbf{m}_p)^T \mathbf{C}_M^{-1} (\mathbf{m} - \mathbf{m}_p) \right\} \quad (1)$$

where $\mathbf{g}(\mathbf{m})$ represents a forward operator of the receiver function (RF) or surface wave phase dispersion (SF), \mathbf{d} is the vector of observations (data), \mathbf{m} is the model-parameter vector, and $*$ and T denote complex conjugate and transpose, respectively. The subscript p denotes a priori information, and \mathbf{C}_{RF} and \mathbf{C}_{SF} are covariance matrix of the receiver functions and phase dispersions, respectively, and \mathbf{C}_M denotes the covariance matrix of the receiver model.

Eq. (1) is optimized with a conjugate gradient method¹²⁻¹³. Simultaneously, a stepwise frequency-expansion is performed in the spectral domain. The forward problem of the complex spectral ratio between the radial and vertical component of RF is calculated using the reflectivity method¹⁴. The phase-velocity dispersion is

solved with a modified version of the fast generalized R/T method proposed by Pei et al.¹⁵⁻¹⁶. We note that the onset-amplitude ratio between the vertical and radial component of RF is fitted upon inversion, because its value is related to the absolute velocity near the surface.

Since not only the magnitude of receiver function and phase dispersion, but also the converging rates of the misfits between predicted and observed data are different, coordination between them is necessary for joint inversion. This is realized by using the formulas

$$vc = vr/avr + p(vp/avp) \quad (2)$$

and

$$p = (vr \bullet avp)/(vp \bullet avr) \quad (3)$$

where vr and vp are the root-mean-square error of RF and phase dispersion, respectively, and where avr and avp denote the arithmetic average of the observed RF amplitude spectra and of the observed phase-velocities over different periods, respectively. We note that eq. (3) is used only in the first iteration of the inversion, and the iteration process will be terminated when vc reaches a minimum.

As illustrated in Fig. S1, numerical tests demonstrate that the joint RF-ANT inversion results are not sensitive to the initial model and that model parameters can be retrieved, even for a simple 1-D (layered) starting model. Fig. S1 also suggests that shear wavespeed is best constrained for depths less than 80 km.

2. Data Processing: Fig. S2 depicts the geological framework of our study region as well as the location of the Movable Western Sichuan (MWS) array of 288 broadband stations that provided the data used in this study. Each station was equipped with a Guralp CMG-3ESPC seismometer and a REFTEK-130B01 recorder. Fig. S2 depicts also the lines of section shown and discussed hereinafter: AA', BB', CC', EE', and CD (purple dash lines) as well as the seismic refraction profile¹⁷ (green dash line, coinciding with profile BB') shown in Fig. S12.

Fig. S3 shows the distribution of teleseismic events used. RFs were extracted from teleseismic P waveforms using an iterative deconvolution technique¹⁸. Fig. S4

shows the receiver functions for different azimuths for each of the 19 stations that are located along profile AA' (~31°N) and, as an example, in Fig. S5 we present the RFs with back azimuth for station S16 (Fig. S2, white triangle). In Fig. S4 each trace shown is a stack of RFs for a 5° back azimuth bin, and the traces in Fig. S5 are stacks over 1° back azimuth bins. This stacking suppresses the effects of near-receiver scatter and mitigates the predominance of the best-sampled orientations. Fig. S4 reveals clear Ps conversions (near 5.8 s) below stations S11 to S19, that is, near and east of the Longmenshan fault (mostly in Sichuan Basin), but (with the exception of station S02) well defined Ps conversions are absent west of station S11, that is, beneath the plateau.

Theoretically, the time delay of the Ps conversion after the onset of the P arrival for the stratified crustal media can be calculated from¹⁹

$$\Delta t_{ps} = t_{ps} - t_p = \frac{h}{V_p} \left[\sqrt{K^2 - (cV_p)^2} - \sqrt{1 - (cV_p)^2} \right], \quad (4)$$

with $K = V_p/V_s$ and $c = 1/V_p^*$,

and the depth, h , where the conversion occurs (that is, the layer – or, in our case, crustal – thickness) can be estimated approximately from²⁰

$$h \approx (V_p \Delta t_{ps}) / (K - 1), \quad (5)$$

where V_p and V_s denote the velocity of the P- and S-wave, respectively. In eq. (4), V_p^* denotes the apparent P-wave velocity. Thus, the time delay of the Ps conversion after the onset of the P arrival increases linearly with the layer thickness.

Liu & Shao²¹ and Liu & Kind²⁰ investigated the relationship between the nature of the interface and the amplitude of the Ps conversion using generalized ray theory²² and the reflectivity method²³, respectively. These studies indicate that simple model perturbations of the Moho transition zone can significantly alter the amplitude of the Ps conversions. Especially, a gradual transition can greatly reduce the amplitude of the Ps conversion at the Moho. For dip angles less than 20°, dipping interfaces have little effect on the amplitude and arrival time of the Ps conversions²⁴. Based on these results, Fig. S4 suggests that beneath the eastern Tibetan Plateau (west of station S11) the crust-mantle boundary is not sharp but gradual. Identification of Moho

conversions (and, thus, a Moho itself) is then difficult, if not impossible. Therefore, we depict a transition interval instead of a specific Moho estimate.

Fig. S6 shows cross-correlations of ambient seismic noise recorded at the MWS array, which were obtained by summation of 10-day long vertical-component ambient seismic noise records. Technical details of data processing can be found in [25, 26]. A preliminary study²⁶ presented Rayleigh-wave phase-velocity maps of only half of the MWS array (156 stations) and did not invert for variations in shear speed.

3. Comparison with RF inversion: Here, we compare for 19 stations along profile AA' (see Fig. S2) the results from RF and joint RF-ANT inversion. We note that the difference in epicentral distance of the events used for each station is less than 20°.

Fig. S7 shows Rayleigh phase-dispersion at stations S01-S19 (Fig. S2, white triangles), measured using the method due to Yao et al.²⁵. The region beneath the MWS array is parameterized using a 0.2° × 0.2° grid, and the phase velocities at periods from 2 to 40 s at each station were determined through linear interpolation.

Fig. S8 shows the waveform fits from the joint RF-ANT and the non-linear RF Complex Spectrum Ratio (CSR) inversion²⁷, respectively. As an example, Fig. S9 shows the fit for station S16 after joint RF-ANT inversion. Fig. S10 depicts 1D shear wavespeed profiles beneath S01-S19 from RF-ANT inversion. This result suggests that in the Songpan-Ganze unit the crust-mantle transition is gradual, with crust-like low wavespeeds extending to relatively large depths, whereas beneath Sichuan Basin the transition from crust-like wavespeeds to typical mantle values is sharp.

Fig. S11 shows seismic sections along AA' from joint RF-ANT and RF-CSR inversion, respectively. For the purpose of this comparison, both sections were obtained by lateral linear interpolation between stations—as opposed to Fig. 3a (main text), which is a slice along AA' through the 3D model. Fig. S11 shows that the structures inferred with these two methods are quite different, which could lead to different geological interpretations.

4. Seismic sections across Eastern Tibetan plateau: Fig. S12 compares the 2D seismic refracted section due to Wang et al.¹⁷ with results from our 3D inversion

(profile BB', ~30°N). Noting that the sections depict P- and S-wavespeed variations, respectively, these independent observations agree well each other, except that our results suggest that the crust-mantle transition beneath the Kangding unit is gradual.

Profile CC' just west of the Longmenshan fault (Fig. S13a) shows that crust and upper mantle structures of the Kangding and Songpan units are quite different, with anomalous low-wavespeeds in the upper mantle beneath the latter. Profile CD across the Lijiang fault (Fig. S13b) shows that the Kangding and Dianzhong units have clearly different (lower) crustal thickness and velocities. These observations are confirmed by wavespeed variations beneath stations S20 and S21 (Fig. S14).

Fig. S15 shows the structure along EE', which is perpendicular to the Longmenshan faults and coincides with the southern part of the profile given by Zhang et al.²⁸. Both results reveal eastward thickening of the transitional lower crust as well as low-velocity anomalies at upper mantle depths beneath the Songpan-Ganze unit. Fig. S15 also suggests that the drop of elevation between the Longmenshan and Sichuan basin does not coincide exactly with the onset of crustal thickening towards the Tibetan plateau. This observation agrees with Wang et al.²⁹ and Robert et al.³⁰ and is consistent with a (steep) westward dip of the Longmenshan fault. In contrast to these earlier studies, however, we interpret the slow anomalies at upper mantle depths beneath the Songpan-Ganze unit (Fig. S15) as part of a complex crust-mantle transition and not as evidence for a lithosphere-asthenosphere boundary.

In Fig. S16, we compare the results from our inversions of dense seismic array data with cartoons illustrating the concept of the “channel flow model” due to Royden and co-workers³¹⁻³². Figs. S16a and S16b indicate that (i) flat plateau topography is underlain by seismically slow (and thus, probably, mechanically weak) crust and that (ii) the steep topography at Longmenshan (Fig. S16a) coincides with a stark contrast between low wavespeed anomalies in the weak plateau crust and strong Sichuan basin crust, whereas further south (Fig. 16b) a continuous zone of anomalously low wavespeed (and, probably, mechanical strength) underlies the gentle topographic gradient well across the craton boundary and into Yunnan province.

The cartoons in Fig. S16c,d have been used to explain differences in topographic

gradients through lateral variations in rheology of the crust³¹⁻³²: steep topographic relief forms if weak (middle or lower) crust can not flow sideways because adjacent crust is too strong (Fig. S16c), whereas the topographic gradient is expected to be small if weak crust can flow laterally into adjacent weak crust (Fig. S16d). Our results indicate substantial lateral variation in such flow and suggest that the style of deformation of the Eastern Tibetan Plateau is not controlled either by crustal flow or lateral sliding of undeformed rigid blocks but that strain partitioning results from the interplay between localized crustal flow and major faults.

References and Notes

- 1 Ammon, C. J., Randall, G. & Zandt, G. On the non-uniqueness of receiver function inversions. *J. Geophys. Res.* **95**, 15303–15318 (1990).
- 2 Ozalaybey, S., Savage, M. K., Sheehan, A. F. Louie, J. N. & Brune, J. N. Shear-wave velocity structure in the northern Basin and Range province from the combined analysis of receiver functions and surface waves. *Bull. Seism. Soc. Am.* **87**, 183–199 (1997).
- 3 Julia, J., Ammon, C. J., Herrmann, R. B. & Correig, A. M. Joint inversion of receiver function and surface wave dispersion observations. *Geophys. J. Int.* **143**, 1–19 (2000).
- 4 Sung, J. C., Chang-Eob, B. & Langston, C. A. Joint analysis of teleseismic receiver functions and surface wave dispersion using the Genetic algorithm. *Bull. Seism. Soc. Am.* **94**, 691–704 (2004).
- 5 Lawrence, J. F. & Wiens, D. A. Combined receiver-function and surface wave phase- velocity inversion using a niching genetic algorithm: application to Patagonia. *Bull. Seism. Soc. Am.* **94**, 977–987 (2004).
- 6 Lobkis, O. I. & Weaver, R. L. On the emergence of the Green's function in the correlations of a diffusive field. *J. acoust. Soc. Am.* **110**, 3011–3017 (2001).
- 7 Weaver, R. L., & Lobkis, O. I. Diffuse fields in open systems and the emergence of the Green's function. *J. acoust. Soc. Am.* **116**, 2731–2734 (2004).
- 8 Campillo, M. & Paul, A. Long-Range correlations in the diffuse seismic coda. *Science*, **299**, 547–549 (2003).
- 9 Shapiro, N. M. & Campillo, M. Emergence of broadband Rayleigh waves from correlations of the ambient seismic noise. *Geophys. Res. Lett.* **31**, 1615–1619 (2004).
- 10 Shapiro, N. M., Campillo, M., Stehly, L. & Ritzwoller, M. H. High-resolution surface-wave tomography from ambient seismic noise. *Science* **307**, 1615–1618 (2005).
- 11 Liu, Q. Y. et al. Joint inversion of receiver function and ambient noise based on Bayesian theory. *Chin. J. Geophys.* **53**, 961–972 (2010).

- 12 Tarantola, A. *Inverse Problem Theory, methods for data fitting and model parameter estimation* (Elsevier, Amsterdam, 1987).
- 13 Tarantola, A. *Inverse Problem Theory and Methods for Model Parameter Estimation* (SIAM, PA 19104- 2688 USA, 2005).
- 14 Müller, G. The reflectivity method: a tutorial. *J. Geophys.* **58**, 153-174 (1985).
- 15 Pei, D. H., John, N. L. & Pullammanappallil, S. K. Improvements on computation of phase velocities of Rayleigh waves based on the generalized R/T coefficient method. *Bull. Seism. Soc. Am.* **98**, 280–287 (2008).
- 16 Pei, D. H., John, N. L. & Pullammanappallil, S. K. Erratum to Improvements on Computation of Phase Velocities of Rayleigh Waves Based on the Generalized R/T Coefficient Method, *Bull. Seism. Soc. Am.* **99**, 2610–2611 (2009).
- 17 Wang, C. Y., Han, W. B., Wu, J. P., Lou, H. & Chan, W. W. Crustal structure beneath the eastern margin of the Tibetan Plateau and its tectonic implications. *J. Geophys. Res.* **112**, B07307 (2007).
- 18 Ligorria, J. P. & Ammon, C. J. Iterative deconvolution of teleseismic seismograms and receiver function estimation. *Bull. Seism. Soc. Am.* **89**, 1395–1400 (1999).
- 19 Pameranceva, E. V. & Mozzenko, A. N. *Seismic investigations with equipment of “Earth”*, (Nedra, Moscow, 1977) (in Russian).
- 20 Liu Q. Y. & Kind R. Lateral variations of the structure of the crust-mantle boundary from conversions of teleseismic P waves. *J. Geophys.* **60**, 149–156.
- 21 Liu Q. Y. & Shao X. Z. A study of the dynamic characteristics of PS converted waves with the synthetic seismograms. *Acta Geophysica Sinica* **28**, 291–302 (1985) (in Chinese with English abstract).
- 22 Wiggins, R. A. & Helmberger, D. V. Synthetic seismogram computation by expansion in generalized rays. *Geophys. J. R. astr. Soc.* **37**, 73–90 (1974).
- 23 Kind, R. The reflectivity method for different source and receiver structures and comoparison with GRF data. *J. Geophys.* **58**, 146–152 (1985).
- 24 Chen, J. H & Liu Q. Y., Wavefield features of teleseismic receiver function in laterally inhomogeneous media. *Acta Seismologica Sinica* **13**, 656–663 (2000).
- 25 Yao, H. J., R.D. Hilst van der & de Hoop, M. V. Surface-wave array tomography

- in SE Tibet from ambient seismic noise and two-station analysis—I. Phase velocity maps. *Geophys. J. Int.* **166**, 732–744 (2006).
- 26 Li, Y. et al. Phase velocity array tomography of Rayleigh waves in western Sichuan from ambient noise. *Chin. J. Geophys.* **53**, 842–852 (2010) (in Chinese with English abstract).
- 27 Liu, Q. Y., Kind, R. & Li, S. C. Maximal likelihood estimation and nonlinear inversion of the complex receiver function spectrum ratio. *Chin. J. Geophys.* **39**, 502–513 (1996) (in Chinese with English abstract).
- 28 Zhang, Z. et al. Seismic signature of the collision between the east Tibetan escape flow and the Sichuan Basin. *Earth Planet. Sci. Lett.* **292**, 254–264 (2010).
- 29 Wang Y., Mooney, W. D., Yuan, X., Okaya N. Crustal Structure of the Northeastern Tibetan Plateau from the Southern Tarim Basin to the Sichuan Basin, China. *Tectonophysics* **584**, 191–208 (2013).
- 30 Robert, A. et al. Crustal structures in the area of the 2008 Sichuan earthquake from seismologic and gravimetric data. *Tectonophysics* **491**, 205–210 (2010).
- 31 Clark, M. K. & Royden, L. H. Topographic ooze: building the eastern margin of Tibet by lower crustal flow. *Geology* **28**, 703–706 (2000).
- 32 Clark, M. K. Late Cenozoic Uplift of Southeastern Tibet. PhD dissertation, Massachusetts Institute of Technology (2003).

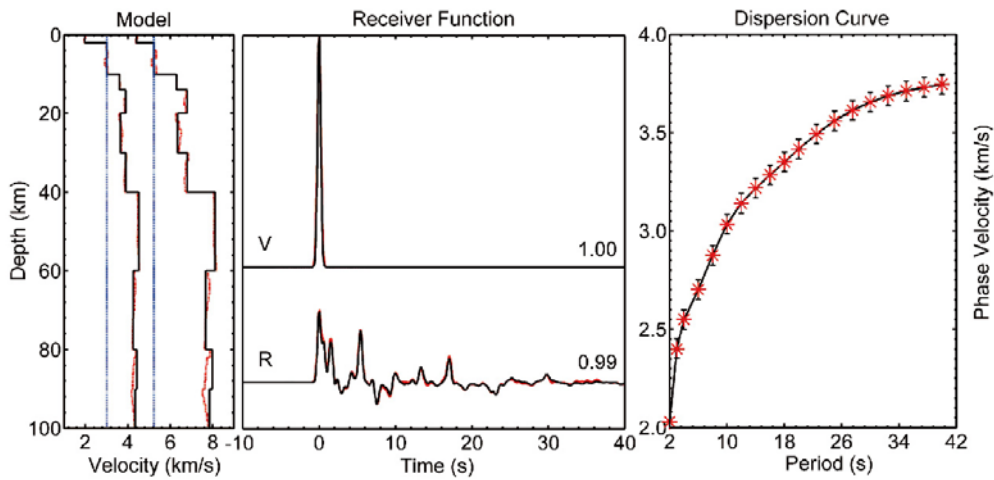


Fig. S1. Numerical test on the joint RF-ANT inversion. Left: Receiver model, where black solid lines represent the P- and S-velocity of the “true” model, respectively. Blue dot lines are the initial model, and red dash lines are the inversion model. Middle: Receiver function, where black lines are “true” receiver functions and red line is the inversion result. V and R denote the vertical and radial component, respectively, and the digits on the right are correlation coefficients. Right: Phase-dispersion curves, where black solid lines with error bars are the “true” phase-dispersion curve of Rayleigh waves and the red stars are the phase-velocities at each period by the inversion.

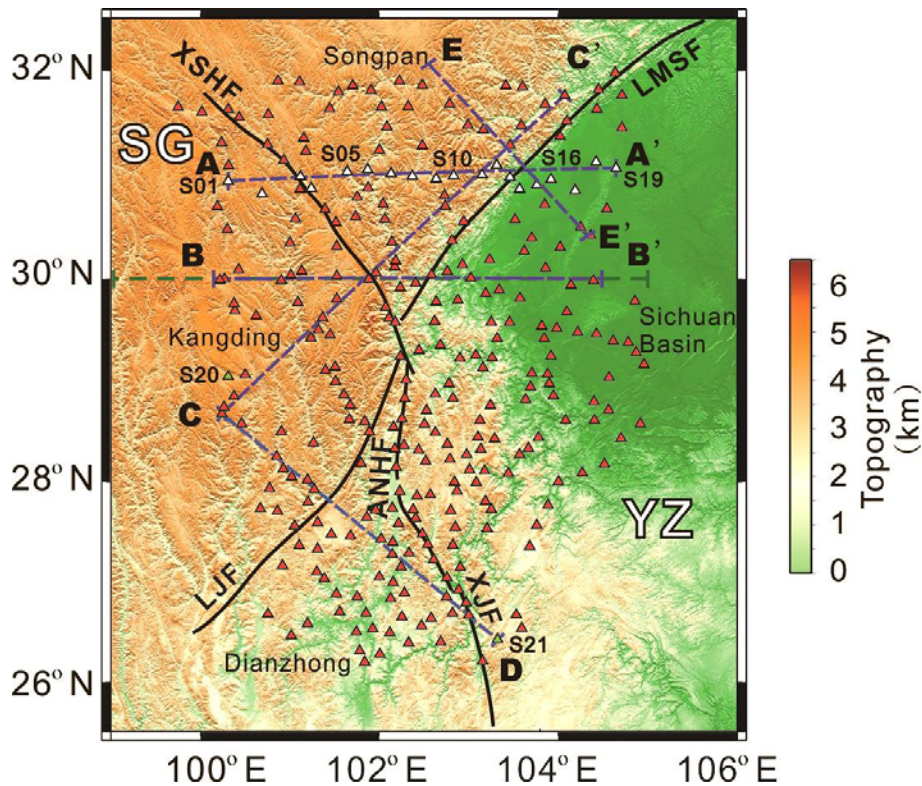


Fig. S2. Station map: movable western Sichuan seismic array. Black solid lines denote boundary faults. Red and white triangles denote seismic stations. S01~S19 indicate the station codes with white triangles along the 31°N profile. S20 and S21 indicate

the codes of stations (green triangle). Blue dash lines denote receiver function profiles. Green dash line denotes seismic refraction profile¹⁷. LMSF: Longmenshan fault; XSHF: Xianshuihe fault; LJF: Lijiang fault; ANHF: Anninghe fault; XJF: Xiaojiang fault. SG: Songpan-Ganze unit; YZ: Yangze craton.

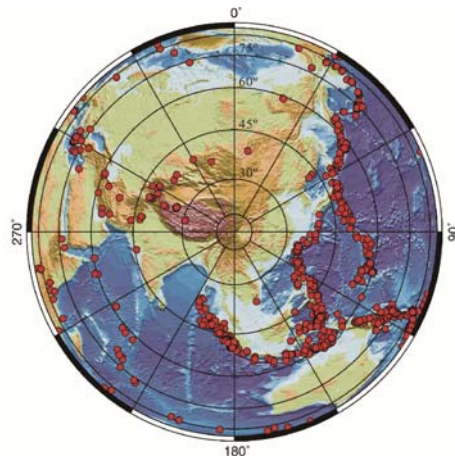


Fig. S3. Events used in this study. Red circles represent the events used. The center is located on the movable western Sichuan seismic array.

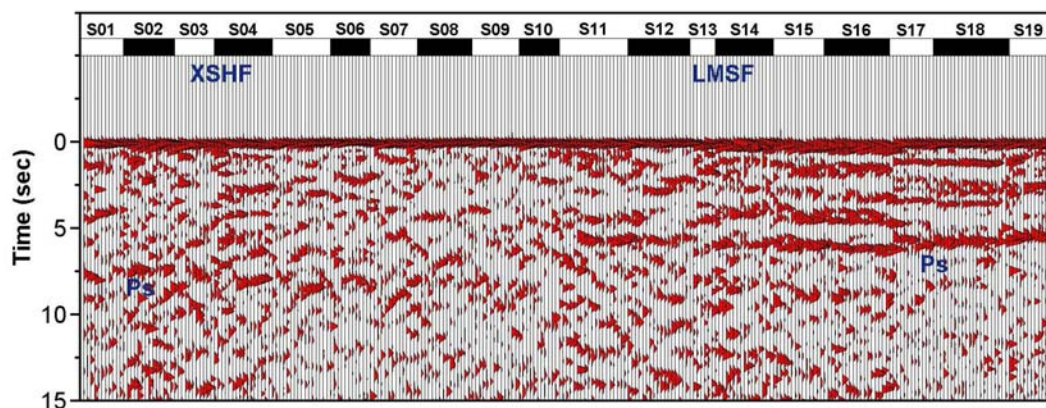


Fig. S4. Receiver function profile along 31°N (profile AA'). Each trace of the receiver function is a stack of RFs for a 5° back azimuth bin. S01-S19 denotes the station codes. Black-white stripe depicts the range of the receiver functions at each station. LMSF and XSHF indicate the position of the Longmenshan fault and Xianshuihe fault, respectively. The red color describes the positive half cycles of the receiver function and their negative part has been cut off. The receiver functions at each station are arranged in accordance with the back azimuth increasing from left to right. Ps denotes the P to S conversion at the Moho discontinuity.

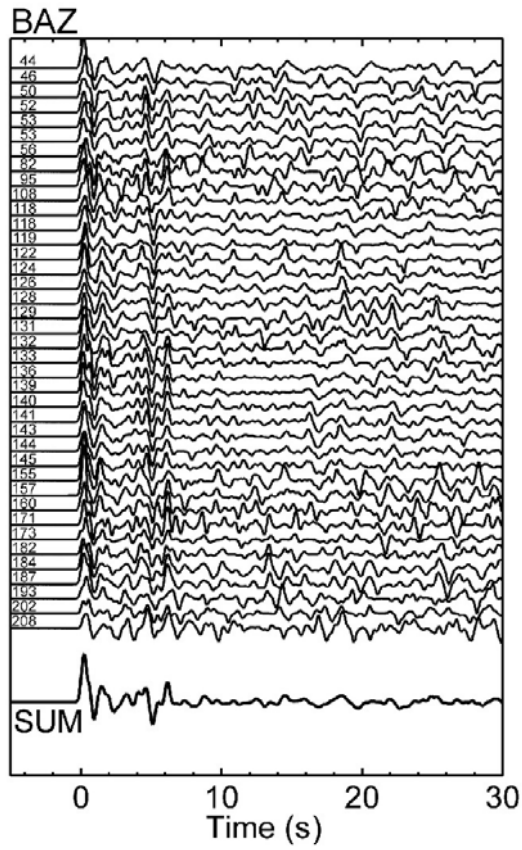


Fig. S5. Radial components of receiver functions over different azimuths at Station S16. BAZ denotes back azimuth. Sum denotes the summation over all of back azimuths.

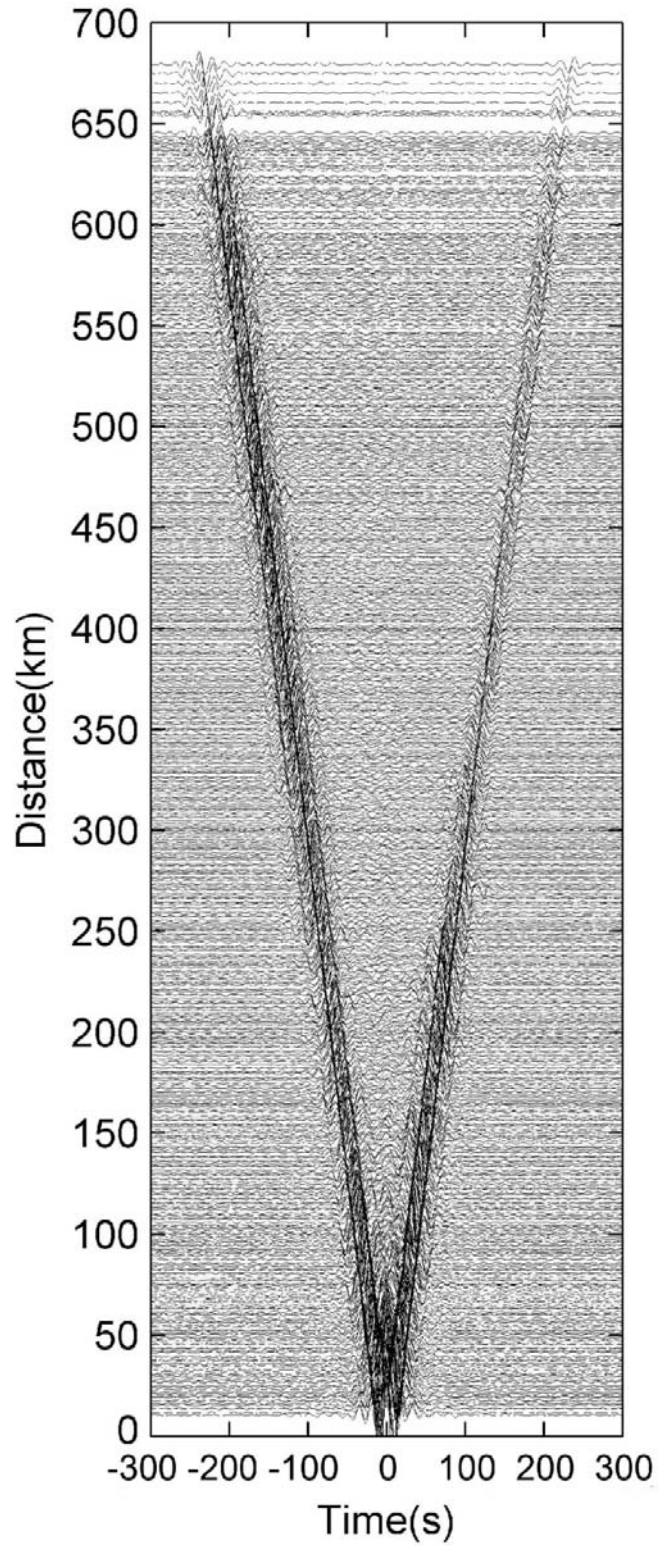


Fig. S6. Cross-correlations of ambient seismic noise recorded by the the movable western Sichuan seismic array. They are the results passed through 0.1 Hz low-pass filter. Distance: space of station pair.

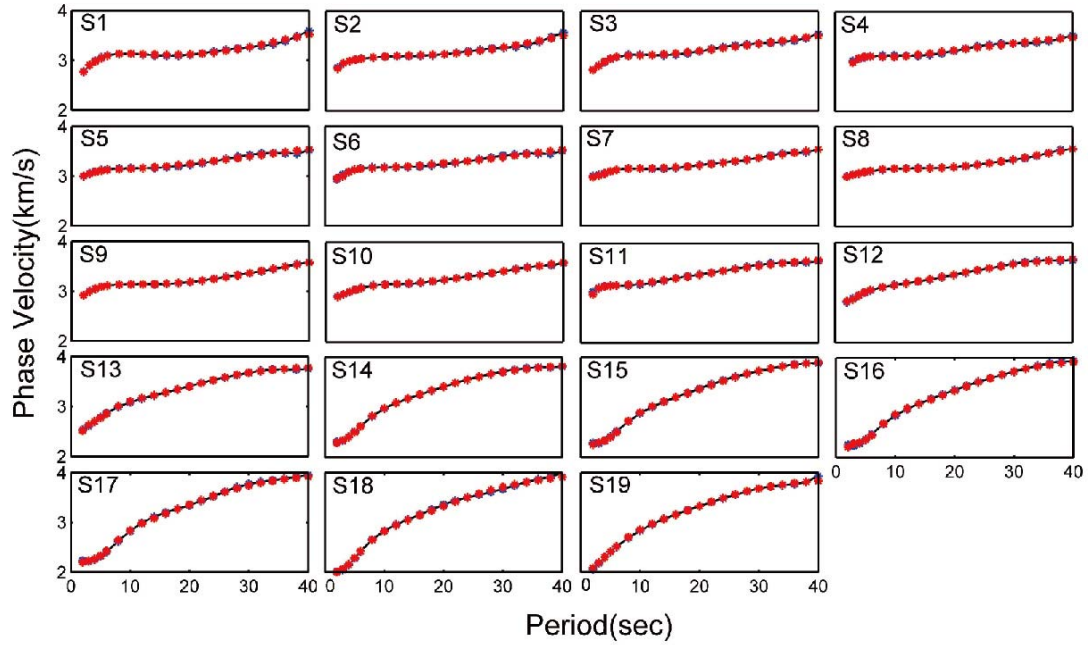


Fig. S7. Rayleigh-wave phase-dispersions at Station S01-S19. Black and red solid dots denote the observed and predicted results, respectively.

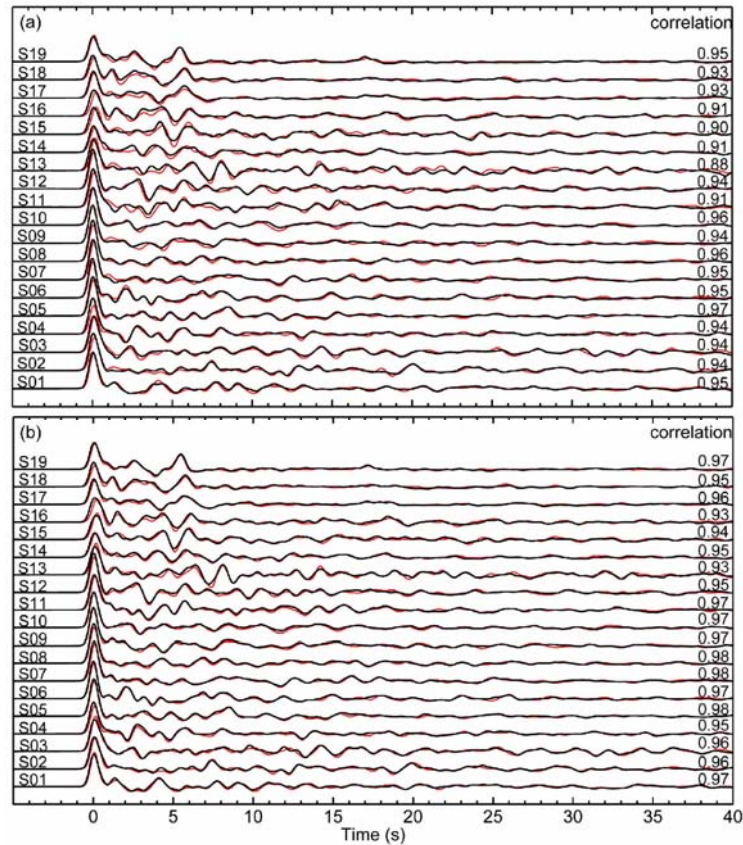


Fig. S8. Waveform fitting of the predicted and observed RFs. (a) by the joint RF-ANT; (b) by the CSR inversion. Black and red solid lines show the predicted and observed RFs, respectively. On the left are the station codes, and on the right are the correlation coefficients between the predicted and observed RFs.

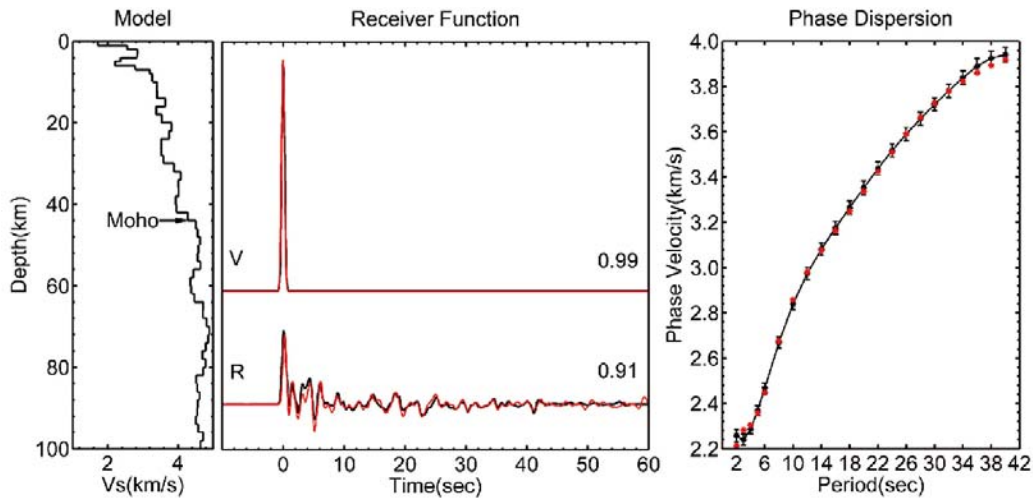


Fig. S9. The results at Station S16 by the joint RF-ANT inversion. Left: Shear-wave velocity model; Center: RF waveform fits; Black and red solid line represent the predicted and observed RF, respectively; The numbers on the right are the correlation coefficient between the predicted and observed RF; Right: Black line with error-bar denotes the observed Rayleigh wave phase dispersion curve; Red dots are the predicted phase velocities at each period.

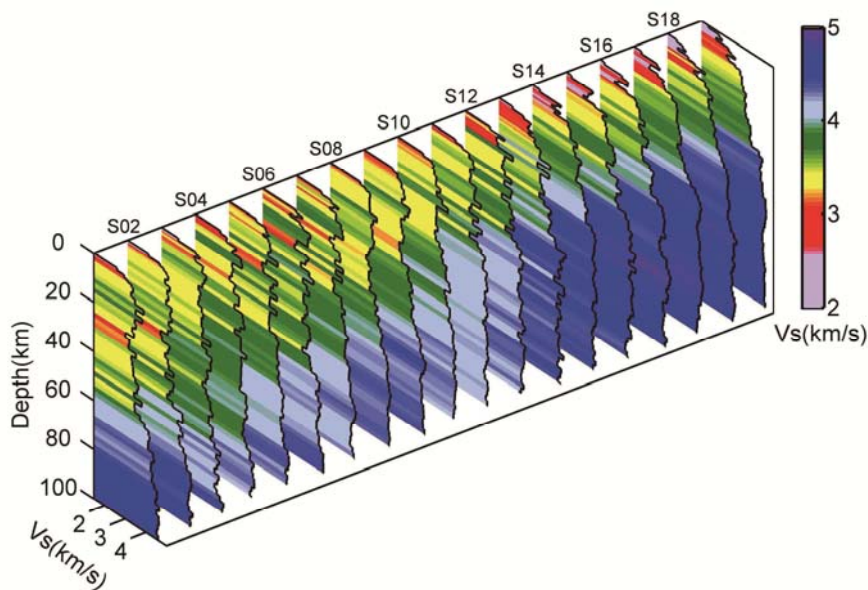


Fig. S10. Shear-wave velocity models beneath Station S1-S19 obtained from the joint RF-ANT inversion.

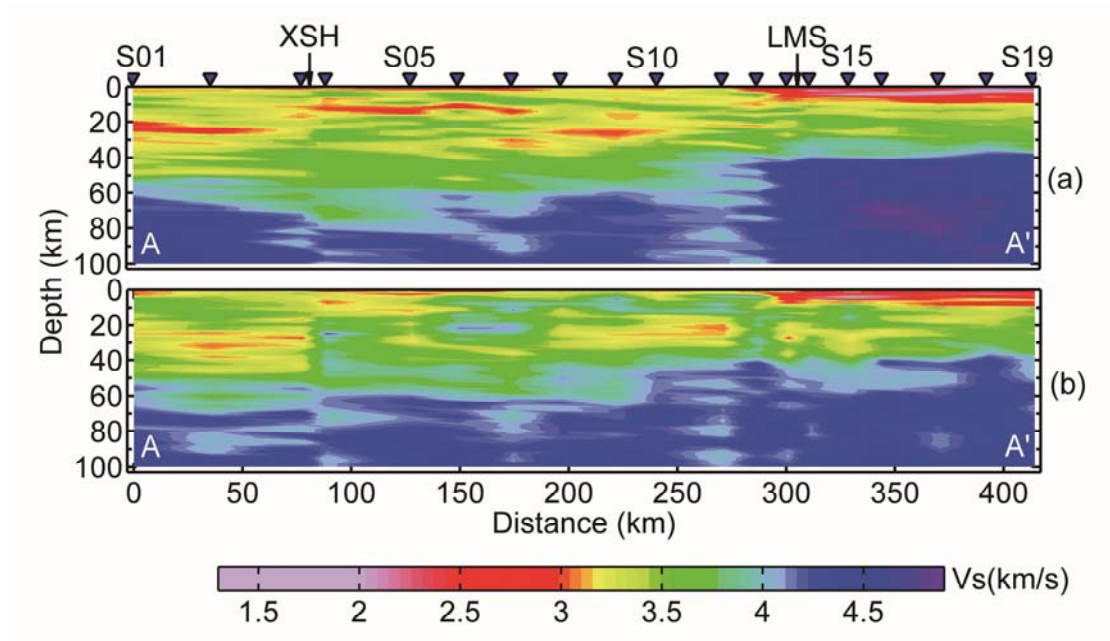


Fig. S11. Seismic section along Station S01-S19 (profile AA'). Upper part: the result by the joint RF-ANT inversion; Lower part: the result by the CSR inversion. Acronyms as in Fig.S2

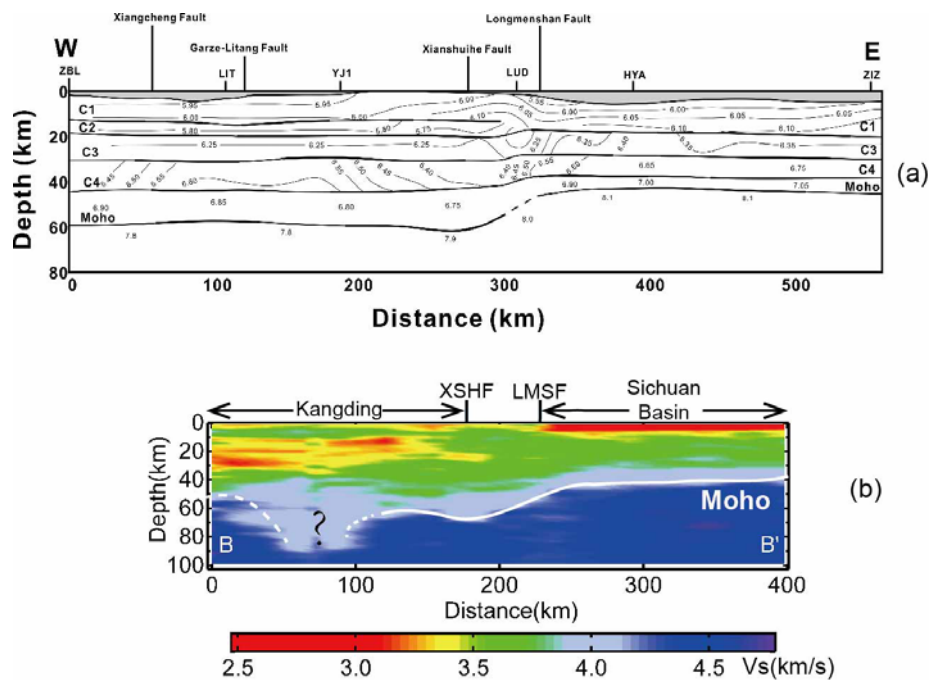


Fig. S12. Comparison with seismic refraction survey. (a) seismic refracted section of the P-wave velocity along the latitude of 30°N ¹⁷; (b) slice of seismic RF cross-section of the S-wave velocity along the latitude of 30°N . White solid line depicts the Moho, and white dash line indicates areas where the crustal boundary is not well defined in the receiver functions. The question mark denotes that the Moho could be disappear. Acronyms as in Fig. S2.

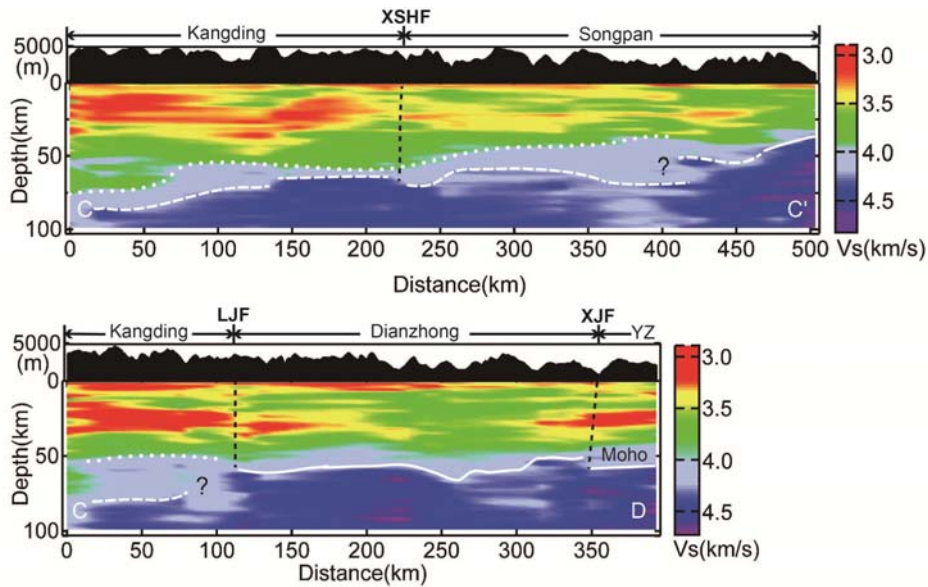


Fig. S13. Slices of seismic RF cross-section across the eastern Tibetan plateau. The topography along the profile is shown at the top. The black dash lines depict faults. Solid white lines depict the position of the Moho (crust-mantle boundary) beneath Yangtze craton; white dot and dash lines indicate the top and bottom of a gradational crust-mantle transition beneath the Plateau, respectively. Acronyms as in Fig. S2.

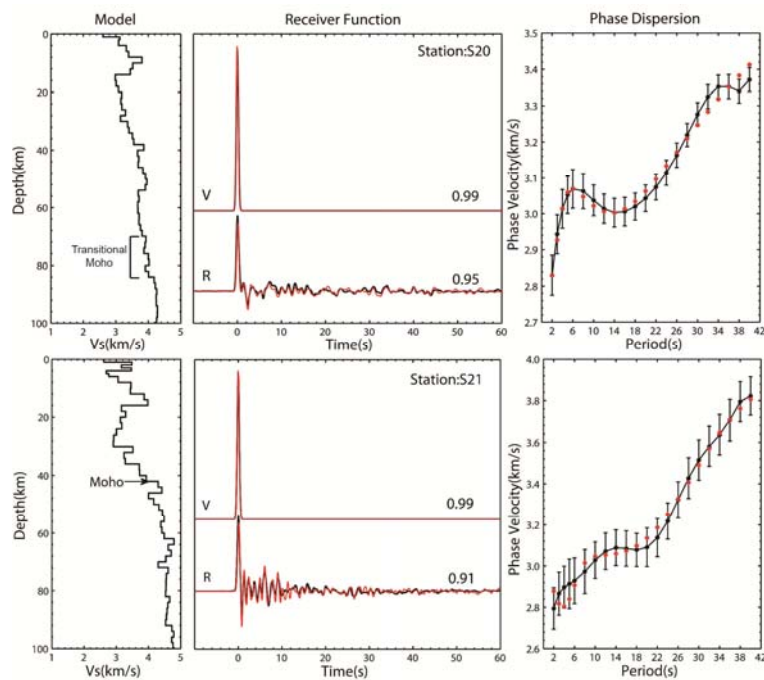


Fig. S14. Results at Station S20 and S21 (station codes in Fig. S2) from joint RF-ANT inversion. Top (S20): example of a station at the Tibetan Plateau, beneath which a Moho cannot be detected unambiguously and where the data suggest that the crust-mantle boundary is transitional rather than discontinuous. Such a transitional Moho is depicted with dashed lines in Fig. 3 of the main text. We note that, if done in isolation, receiver

function analyses might yield different estimates of crustal thickness, which may explain differences between our results and those from receiver function studies. Bottom (S21): example of a station at the Yangze craton, where the Moho has a clear velocity discontinuity. Same notation as Fig. S9.

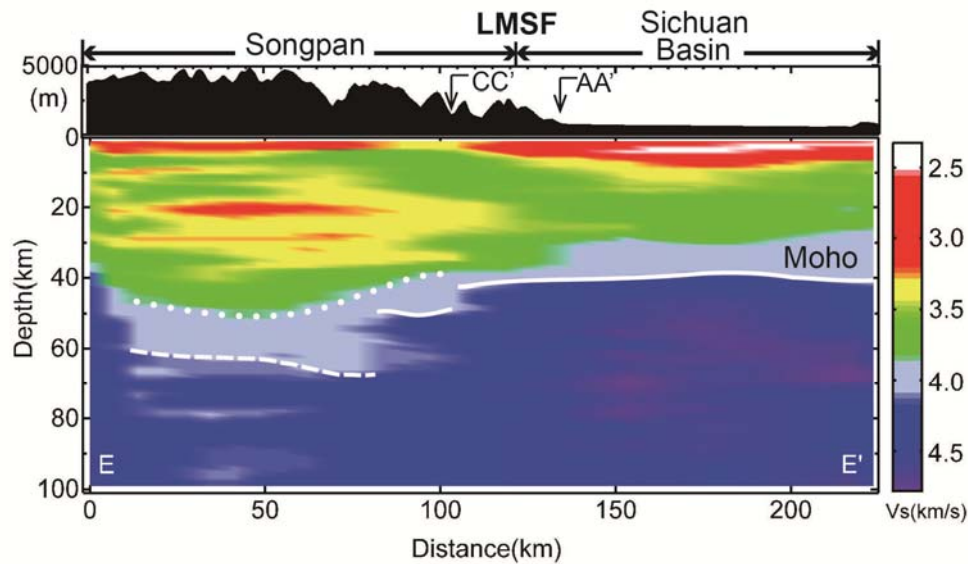


Fig. S15. Slice of seismic RF cross-section across and perpendicular to the Longmenshan faults. The topography along the profile is shown on the top. White solid lines depict our estimates of the base of the crust. White dot and dash lines indicate the top and bottom of a gradational crust-mantle transition beneath the Plateau, respectively (dashed lines depict a transitional Moho). The arrows indicate the position of the profile CC' and AA' (Fig. S2). Acronyms as in Fig. S2.

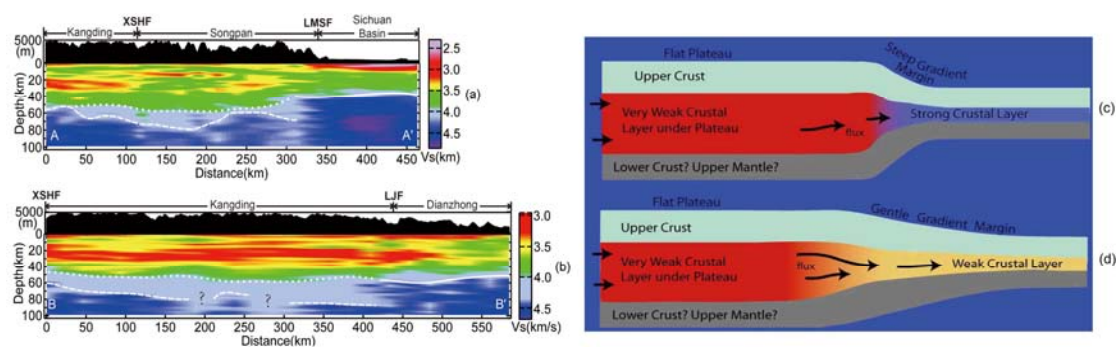


Fig. S16: Comparison of crustal structure constrained by waveform data obtained by a dense seismography array in western Sichuan (a and b) and as envisaged in the canonical channel flow model³¹⁻³² (c and d; courtesy of Prof. L. Royden, MIT). Acronyms as in Fig. S13.